https://doi.org/10.5194/egusphere-2026-507
Preprint. Discussion started: 29 January 2026


# Estimation of wet radome and rain induced attenuation in cloud radar observations

Bernd Mom[1] and Dmitri Moisseev[1,2]

[1]Institute for Atmospheric and Earth System Research (INAR), University of Helsinki, Helsinki, Finland
[2]Finnish Meteorological Institute (FMI), Helsinki, Finland

**Correspondence:** Bernd Mom (bernd.mom@helsinki.fi)

**Abstract.** Estimation of the properties of ice clouds above rain from ground-based cloud radar observations is affected by the wet radome, rain path, and melting layer attenuation. In this study, we present a method for estimating wet radome and rain attenuation using collocated disdrometer observations. To ensure that cloud radar retrievals can be performed at a relatively high temporal resolution, on the order of a minute, attenuation estimates are computed at the same temporal resolution. However, the small sampling volumes of disdrometers introduce significant uncertainty in these estimates. To address this, we developed a statistical model to calculate the uncertainty range of the estimated drop size distribution (DSD) parameters and radar variables. The computed radar variables are compared to radar observations to identify radome attenuation. As an additional check of the validity of the estimated variables, the DSD observations are used to calculate rain intensity and accumulated precipitation, which are then compared to precipitation gauge measurements. In addition to radome attenuation, rain path attenuation is estimated using specific attenuation derived from the disdrometer observations. Limitations of this approach are presented and discussed. The proposed method is demonstrated using observations of two rain events collected in Hyytiälä, Finland. These events were selected to demonstrate the effect of radome attenuation, which was rather minor in one case and as large as 10 dB in the other.

## 1 Introduction

The cloud remote sensing observations carried out at the Aerosol, Clouds and Trace gases Research Infrastructure (ACTRIS) stations provide a comprehensive dataset of cloud properties that span across different climatic zones. The cloud products provided by ACTRIS cloud profiling stations (also known as Cloudnet) range from raw data to multi-sensor cloud microphysical retrievals, such as liquid and ice water contents (Hogan and O'Connor, 2004; Hogan et al., 2006b; Illingworth et al., 2007). These observations can be used to evaluate the cloud representation in numerical weather prediction models (Hogan et al., 2006a), among other things.

The availability of data from certain remote sensors and the associated measurement uncertainties could limit availability of some retrieval products. Currently, there is a significant uncertainty associated with retrievals of ice clouds properties, in ice over rain cases. Uncorrected attenuation caused by a wet radar radome, path attenuation in rain, and attenuation in the melting

https://doi.org/10.5194/egusphere-2026-507
Preprint. Discussion started: 29 January 2026


layer introduce significant errors that make the retrieval of ice cloud properties highly inaccurate (Hogan et al., 2006b). To improve the retrievals of the ice clouds, the above-mentioned attenuation should be estimated and compensated for.

Radome attenuation can be reduced using a radome blower in combination with hydrophobic coating as implemented in some of the newer cloud radar systems (Küchler et al., 2017). However, the hydrophobic coating degrades over time, making radome attenuation an issue, even for systems equipped with blowers. The strength of attenuation depends on the rain intensity and duration (Gorgucci et al., 2013; Kurri and Huuskonen, 2008). For radars operating at W-band wavelengths, this attenuation can be greater than 10 $\mathrm{dB}$ (Myagkov et al., 2020). Additionally, rain path attenuation is strongly influenced by the rain intensity (Williams, 2022; Matrosov, 2008; Lhermitte, 1990). Various methods exist to determine the attenuation in rain (Matrosov, 2007; L'Ecuyer and Stephens, 2002; Hitschfeld and Bordan, 1954). L'Ecuyer and Stephens (2002); Hitschfeld and Bordan (1954) require knowledge of path integrated attenuation, which is not available for a single frequency cloud radar observations. Matrosov (2007) utilizes drop size distributions (DSDs) obtained from a disdrometer to compute attenuation by T-matrix calculations. The last attenuation correction needs to be applied to the melting layer. This has been studied by Li and Moisseev (2019), who presented a technique to derive melting layer attenuation based on multi-frequency radar differential attenuation measurements, as well as by Matrosov (2008), who used a relationship between rain rate and melting layer attenuation. The derived melting layer attenuation parameterizations Matrosov (2008); Li and Moisseev (2019) can be used to estimate this attenuation, but they need rain rate and unattenuated reflectivity values from just below the melting layer.

The standard equipment of the ACTRIS cloud profiling stations consists of a cloud radar, ceilometer, microwave radiometer, disdrometer, precipitation gauge and weather station. Disdrometer observations of DSDs are frequently used in combination with cloud radars, in order to derive radar-based methods to estimate rainfall and precipitation properties (Giangrande et al., 2019; Tridon et al., 2017), or to determine radar calibration offsets (Deng et al., 2024; Myagkov et al., 2020; Kollias et al., 2019; Williams et al., 2005; Lamer et al., 2021). When validating radar-derived rain retrieval methods, disdrometers provide essential data on precipitation characteristics. For radar calibration, the disdrometer serves as a reference, allowing for monitoring differences between the disdrometer-derived reflectivity measurements and the radar observations. The objective of this study is to estimate radome and rain path attenuation at temporal scales of a minute. Since such estimates can be rather uncertain, the validity interval of the estimates should also be computed. The challenge in this type of analysis is the inherent uncertainty of computed radar retrievals from disdrometer observations arising from the relatively small sampling volume. A disdrometer sampling volume is in the order of $10^{-1}$ $\mathrm{m}^3$, whereas a cloud radar observation volume usually exceeds $10^3$ $\mathrm{m}^3$. Disdrometer observations of DSD are typically truncated on smaller and larger diameter sides. Due to smaller sampling volumes, disdrometers tend not to observe larger droplets (Ulbrich and Atlas, 1998). Because the sensitivity of the disdrometer sensors, smaller droplets, typically with diameters less than 0.4 mm, are also not detected (Moisseev and Chandrasekar, 2007). Furthermore, beyond estimating radar retrieval uncertainties, a further challenge lies in comparing disdrometer and cloud radar measurements. This is caused by the difference in the measurement altitudes. As droplets fall from the radar volume to the surface, droplets are affected by processes such as evaporation and collision-coalescence. These processes modify the DSD affecting the comparison between radar retrievals.

https://doi.org/10.5194/egusphere-2026-507
Preprint. Discussion started: 29 January 2026


In this study, DSD observations from disdrometer are used to calculate radar reflectivity values, to estimate radome attenuation and rain path attenuation. The uncertainty range of disdrometer based estimates of radar variables are also computed. To compute the uncertainty range, a forward model of the disdrometer observations is used. This model takes into account the sampling characteristics of a disdrometer that is used for DSD observations. It is proposed that the rain path attenuation can be mitigated by using specific attenuation computed from DSD observations. This approach is constrained by factors such as rain evaporation and increased precipitation intensity due to embedded clouds. A method for diagnosing such cases is also presented.

The method is illustrated on data collected at the University of Helsinki Station for Measuring Ecosystem-Atmosphere Relations II (SMEARII) ACTRIS cloud remote sensing station (Hari and Kulmala, 2005), located in Hyytiälä, southern Finland, during rain events recorded in the years 2022 and 2023. Measurements are collected using a collocated Parsivel$^2$ disdrometer, weighing precipitation gauge, vertically pointing W-band Doppler cloud radar and weather station. The method is illustrated on two case studies. One case is selected to have minimal radome attenuation and one case shows strong radome attenuation.

## 2 Data

This study is based on measurements collected at the University of Helsinki Station for Measuring Ecosystem-Atmosphere Relations (SMEARII) located in Hyytiälä Finland (61.844°N, 24.287°E) (Hari and Kulmala, 2005). As an ACTRIS cloud profiling station, SMEARII is equipped with standard instruments consisting of a disdrometer, ceilometer, 94 GHz cloud radar, two precipitation gauges, weather station, and microwave radiometer. The cloud profiling instrumentation is located on the lake Kuivajärvi shore, about 30 m (150 m above mean sea level) below the base of the SMEAR II mast, where the majority of the SMEARII observations are collected. Meteorological data used in this study were collected at the radar field at an altitude of 1.5 m or 151.5 m AMSL, and at multiple heights on the SMEAR II mast. Two rain events that occurred on 26 May 2022 (Moisseev et al., 2025a) and 28-29 July 2023 (Moisseev et al., 2025b) are used to illustrate the presented methodology. In addition, disdrometer observations have been used to present a climatology of DSD parameters over the period 2014-24 (Moisseev and Petäjä, 2025).

### 2.1 Radar

A zenith pointing 94 GHz dual-polarization frequency modulated continuous-wave Doppler cloud radar (HYytiälä Doppler RAdar, HYDRA-W) (Küchler et al., 2017) is used in this study. The radar is equipped with two antennas that have an aperture of 500 mm and a beam width of 0.50°. HYDRA-W uses 3 chirps, but only the two lowest ones are utilized since the proposed method applies solely to rain below the melting layer, which these two chirps cover. The first chirp is used for measurements below 996 m with a range resolution of 25.5 m, while the second chirp covers ranges from 996 m to 3577 m, maintaining the same range resolution. The temporal resolution of the radar observations is 3.35 s.

https://doi.org/10.5194/egusphere-2026-507
Preprint. Discussion started: 29 January 2026


### 2.2 Disdrometer

An OTT ParSiVel$^2$ laser disdrometer (hereafter Parsivel, Tokay et al., 2014; Löffler-Mang and Joss, 2000) is used for DSD observations. The drops are detected using a laser with a wavelength of 650 $\mathrm{nm}$ that covers an area of 180 x 30 $\mathrm{mm}$ (length x width), resulting in a measurement area of 54 $\mathrm{cm}^2$. As droplets cross the laser beam, both their size and fall speed are recorded. These measurements are subsequently categorized into one of the 32 predefined size and velocity classes. The classification of drop sizes depends on whether the type of precipitation is in a liquid or solid state. The lowest and highest measurable range of drop sizes measured for liquid precipitation ranges from 0.2 $\mathrm{mm}$ to 8.0 $\mathrm{mm}$, while for solid precipitation the range is from 0.2 $\mathrm{mm}$ to 25.0 $\mathrm{mm}$. The minimum detectable drop size is 0.312 $\mathrm{mm}$ (class 3), thereby placing the two smallest classes outside the instrument's detectable range. The lowest and highest classes for the fall speed of drops range from 0.2 $\mathrm{m\,s^{-1}}$ to 20.0 $\mathrm{m\,s^{-1}}$. In both the size and velocity classes, the bin width incrementally increases every 5 classes starting at class 10. The bin width begins at 0.125 $\mathrm{mm}$ for the smallest diameters, and subsequently doubles every 5 classes, reaching up to a width of 2.0 $\mathrm{mm}$. The width of the two largest classes is 3.0 $\mathrm{mm}$ (OTT HydroMet GmbH, 2017). Furthermore, this study uses the categorization of precipitation type by precipitation codes, the number of detected particles, the number density, the drop velocity distribution and the raw data.

Accurate estimation of rainfall DSD parameters from Parsivel observations requires enough data to ensure statistical reliability and representativeness. The proposed method applies only to rain and drizzle cases. Consequently, observations are filtered using SYNOP precipitation codes, codes 51–53 for drizzle; 57-58 for drizzle with rain; and 61–63 for rain, as defined in Table 4680 (OTT HydroMet GmbH, 2017, Appendix D). To ensure accurate DSD parameter estimation, a minimum threshold for the number of detected particles is set. This guarantees that a sufficient number of droplets is present across as many drop size classes as possible. In this study, the threshold is set at 100 particles. For the same purpose, droplets should be present in at least five consecutive size classes without falling more than two classes beyond this continuity. Size classes not meeting this criterion are removed. As Parsivel disdrometers are less sensitive to smaller droplets, size classes with median diameters below 0.4 mm are omitted. A closer examination of the remaining data revealed certain features that are not consistent with those of rain, such as insects or side fallers, which deviate in size and fall velocity from typical drops. Raindrops follow a specific velocity-size relationship, as defined by Atlas et al. (1973). A limit is set at the 0.5–1.5 percentile of this velocity-size curve for retaining size and velocity classes, with any falling outside being discarded.

### 2.3 Precipitation gauge

The OTT Pluvio$^2$ weighing precipitation gauge with an opening diameter of 400 $\mathrm{mm}$ was used for precipitation observations during the two analyzed events. The gauge uses a double alter wind shield to minimize the impact of wind on the observations. The gauge records measurements of the bucket weight in real-time at one minute intervals. From these records, precipitation intensity and accumulation are computed after 5 minute integration.

https://doi.org/10.5194/egusphere-2026-507
Preprint. Discussion started: 29 January 2026


### 2.4 Temperature and humidity observations

Temperature and relative humidity observations were collected at the radar field (1.5 m above ground level), and multiple heights at the SMEARII mast, namely at 16.8 m, 35.0 m, 67.2 m, and 125.0 m AGL. Given the difference in ground levels, the highest altitude temperature and humidity measurements were taken about 151 m above the radar (mast + 26 m elevation). This aligns with the third range gate of the HYDRA-W.

## 3 Methods

### 3.1 Difference in heights of radar and disdrometer sampling volumes

In this study we are comparing radar variables computed from disdrometer observations to radar measurements. While the instruments are collocated, there is a vertical distance between the sampling volumes of the instruments. The lowest radar gate, in our case, is at 102 m. In this section we address the choice of the lowest range gate used for the study and what factors affect comparison of disdrometer and radar observations. There are several factors that should be taken into account before disdrometer and radar observations can be compared. The near-field effect (Sekelsky, 2002) and parallax errors (Sekelsky and Clothiaux, 2002) can affect reflectivity measurements at close ranges. Additionally, droplet evaporation can change DSDs between radar and disdrometer observation volumes.

It is expected that the radar reflectivity values in radar, expressed in dBZ scale, will decrease linearly with height. The slope of this line should be equal to the rain specific attenuation. Analysis of the radar reflectivity profile shows that this is not the case for lowest three range gates (102 m, 127 m and 153 m). At these three gates, the reflectivity profile increases and then begins to decrease after the third gate. The increase between the first and third gates is in the order of 1 dB. This feature is consistently present in most if not all radar reflectivity profiles. Myagkov et al. (2020) have reported a similar feature in other W-band RPG FM-CW cloud radars. Possible explanations could be that the observations are not corrected for the near-field effect (Sekelsky, 2002), parallax errors (Sekelsky and Clothiaux, 2002), or evaporation (Myagkov et al., 2020; Tridon et al., 2017). The radar software computes compensation for the parallax error, i.e. error caused by not a complete overlap of receiver and transmitter antenna beams, by taking into account the distance between the antennas and their beam widths (Sekelsky and Clothiaux, 2002). This correction is about 3 dB for the lowest gate and about 1.3 dB for the third gate. It is assumed that there are no antenna pointing errors. However, a 0.05°pointing error of one of the antennas would increase the correction factor to 4 dB for the lowest gate and 2 dB for the third gate. It should be noted that the correction factor decreases with altitude and can be neglected for the range gate three and higher. We should also point out that the pointing errors could explain the reflectivity behavior in the lowest three gates.

For the HYDRA-W system, W-band radar with 0.5 m antenna reflector, the near-field region extends up to 156 m from the radar (Sekelsky, 2002). So the lowest three gates are located within the near-field. In the near-field the observed reflectivity factor is underestimated. In Sekelsky (2002) equations for computing the reflectivity bias caused by antenna near-field are

https://doi.org/10.5194/egusphere-2026-507
Preprint. Discussion started: 29 January 2026


presented. Using these equations the correction factors were computed. These are 0.14 dB for the first gate and 0.05 dB for the third gate and are too small to explain the observations.

A final explanation for the decrease in reflectivity below the third gate is rain evaporation. To investigate how evaporation affects reflectivity, we extrapolated the DSD measured by Parsivel at ground level to the height of the third gate. This is done by applying the droplet growth equation (Lamb and Verlinde, 2011) to observed temperature and relative humidity profiles, which are measured by weather stations on the mast and radar field.

The impact of evaporation on DSDs can be derived from Maxwell's mass growth law (Lamb and Verlinde, 2011). The mass of a droplet is related to its radius through $m_d = \frac{4}{3}\pi r_d^3 \rho_l$, where $m_d$ and $r_d$ are the mass and radius of the droplet, respectively, and $\rho_l$ is the mass density of liquid water. Hence, Maxwell's law for mass growth can be reformulated in terms of the droplets' radius:

$$rd\frac{dr_d}{dt} = f_v G(s - s_k) \tag{1}$$

where $f_v$ is the ventilation coefficient, $G$ acts as a diffusivity with units $\mathrm{m\,s^{-1}}$ and $s$ along with $s_k$ are the ambient supersaturation and the Köhler function supersaturation, respectively. $s_k$ is assumed to be zero for raindrops. Subsequently, Eq. (1) can be rewritten in terms of the rate of change in radius. The last step involves the derivation of an expression for $dt$, using $v = \frac{dH}{dt}$, where $v$ is the terminal velocity of a droplet in $\mathrm{m\,s^{-1}}$ and $dH$ is the height interval in $\mathrm{m}$. The height interval is set to steps of 10 $\mathrm{m}$, from which the closest height with available temperature and relative humidity data are found. The terminal velocity is assumed to follow the form presented in Atlas et al. (1973) (Eq. (2)), as the droplet is expected to reach its equilibrium terminal velocity near the ground.

$$v = 9.65 - 10.3e^{-0.6D} \tag{2}$$

where $v$ is the terminal velocity in $\mathrm{m\,s^{-1}}$ and $D$ is the diameter of the droplet in $\mathrm{mm}$. The Parsivel bin sizes are adjusted every minute to account for evaporation, which consequently changes the bin sizes and causes a shift in the DSD. It is assumed that evaporation affect only the bin sizes themselves, while the number of particles within each size bin remains constant.

Maxwell's law indicates a preference for growth among smaller droplets, which makes them more susceptible to evaporation. This process leads to a narrower DSD as smaller droplets evaporate more rapidly than larger ones. Using the presented cases, these calculations show a subtle change in the DSD parameters and associated radar variables. For example, the droplet diameter increases by roughly 0.05 $\mathrm{mm}$ for the smallest measurable droplets and in the order of $10^{-3}$ $\mathrm{mm}$ for those measuring 10 $\mathrm{mm}$ at a relative humidity of $75\%$ and temperature of $10°C$. Depending on the DSD, the increase in diameter results in an increase of reflectivity of about 0.7 to 0.2 dB at respectively 10 dBZ and 15 dBZ. These environmental conditions are only present at the beginning of a rain event as rain would increase the relative humidity and decrease evaporation. When the relative humidity is increased to $95\%$ while maintaining the same temperature, the evaporative effect is reduced to approximately 0.1 dB.

https://doi.org/10.5194/egusphere-2026-507
Preprint. Discussion started: 29 January 2026


For the events that are presented in this study, evaporation is negligible. The near-field effect is also too small to explain the observations in the lowest three gates. It is possible that there is a slight pointing error in either or both antennas that lead to a larger parallax effect. This effect is range dependent and will decrease with height. Our computations show that for the third gate changes in the parallax correction factor are less than 1 dB, and therefore in this study radar measurements from the third range gate are used.

### 3.2 Computation of DSD parameters and radar variables

To characterize DSDs, the normalized gamma function (Testud et al., 2001; Illingworth and Blackman, 2002; Bringi and Chandrasekar, 2001) given in the following form is used:

$$N(D) = N_w f(\mu)(\frac{D}{D_0})^{\mu} exp[-(3.67+\mu)\frac{D}{D_0}], \quad where \quad f(\mu) = \frac{6}{3.67^4}\frac{(3.67+\mu)^{\mu+4}}{\Gamma(\mu+4)} \tag{3}$$

where $N_w$ is the intercept parameter of a normalized gamma distribution expressed in $\mathrm{mm}^{-1}\,\mathrm{m}^{-3}$, while $D$ and $D_0$ represent the equivalent volume diameter and the median volume diameter, respectively, both measured in $\mathrm{mm}$. The last parameter is $\mu$ which is a unitless shape parameter of the DSD. The three parameters that characterize the DSD, $N_w$, $D_0$, and $\mu$ (Eqs. (6)), are calculated using the third and fourth moments (Eqs. (4)) of the distribution (Bringi and Chandrasekar, 2001).

$$M^3 = \int_{D_{min}}^{D_{max}} D^3 N(D)\, dD \qquad M^4 = \int_{D_{min}}^{D_{max}} D^4 N(D)\, dD \tag{4}$$

$$D_m = \frac{M^4}{M^3} \qquad \sigma_m = \sqrt{\frac{\int_{D_{min}}^{D_{max}} (D-D_m)^2 D^3 N(D)\, dD}{M^3}} \tag{5}$$

$$\mu = \frac{D_m^2}{\sigma_m^2} - 4 \qquad D_0 = \frac{3.67+\mu}{4+\mu} D_m \qquad N_w = \frac{3.67^4}{6}\frac{M^3}{D_0^4} \tag{6}$$

where $D_m$ is the mass-weighted mean diameter, $\sigma_m$ is the standard deviation of the mass-weighted mean diameter which is a measure of the DSD width.

Computations of radar variables are performed using the PyTMatrix python package (Leinonen, 2014; Mishchenko and Travis, 1994; Mishchenko et al., 1996; Wielaard et al., 1997), using the DSD parameters as input. The DSD integration is performed for $D$ ranging from 0 to $2.5D_0$ (Carey and Petersen, 2015). In addition to reflectivity, the mean Doppler velocity is also computed. The computed and observed mean Doppler velocity were used as an additional check of our computations and validity of the presented disdrometer-radar comparisons. While this comparison is not presented, the agreement between computed and observed mean Doppler velocity is excellent. The mean Doppler velocity is not directly computed by PyTMatrix. It was calculated using the following equation:

https://doi.org/10.5194/egusphere-2026-507
Preprint. Discussion started: 29 January 2026


$$mdv = -\frac{\int_{D_{min}}^{D_{max}} v(D) sin(\theta) \sigma(D) N(D)\ dD}{\int_{D_{min}}^{D_{max}} \sigma(D) N(D)\ dD} \tag{7}$$

where $mdv$ is the mean Doppler velocity, $v(D)$ is the terminal velocity in $\mathrm{m\,s^{-1}}$ of a droplet estimated by Eq. (2) taken from Atlas et al. (1973), $\sigma$ is the radar cross section $\mathrm{m^2}$, and $\theta$ is the elevation angle in $\mathrm{m}$. The integration limits $D_{min}$ and $D_{max}$ are 0 and $2.5D_0$ respectively. The radar cross sections were computed by PyTMatrix and saved as lookup table.

### 3.3 Forward model of disdrometer measurements

In this study the method for computing DSD parameters, radar variables and associated uncertainty range is proposed. This problem can be formulated as follows: for a given DSD observation, what is the corresponding range of true, intrinsic, DSDs. For simplicity sake, we will assume that DSDs follow a Gamma functional form and therefore can be described using three parameters, as presented in the previous section. The intrinsic DSD parameters are "true" parameters describing rainfall that we aim to measure. Because of measurement uncertainties, one intrinsic DSD can correspond to an ensemble of observed DSDs. And vice versa, when we go from the observation space to the intrinsic DSD space, one observed DSD can be linked to an ensemble of intrinsic DSDs.

The forward model that describes disdrometer observations by combining statistical uncertainties of DSD measurements and potential hardware limitations links intrinsic and observation DSD spaces. Within an integration time, the number of observed raindrops is defined by a sampling volume and number concentration of raindrops. The sampling volume is determined by disdrometer technical characteristics. For example, for a Parsivel disdrometer the sampling area is 180 x 30 mm. The sampling volume therefore is equal to the sampling area times raindrop velocity times the integration time. Because the raindrop velocity depends on droplet size, the sampling volume is size dependent. Assuming that the velocity size relation is a power law (Atlas and Ulbrich, 1977), $v(D) = 3.78D^{0.67}$, the expected number of observed droplets during an integration time, $\Delta t_{int}$, for a disdrometer with a sampling area, $A$, can be estimated as

$$N_{tv} = A\Delta t_{int} \int_0^\infty v(D) N(D)\, dD = 3.78 A \Delta t_{int} N_w D_0^{1.67} f(\mu) (3.67+\mu)^{-\mu-1.67} \Gamma(\mu+1.67) \tag{8}$$

where $N_w$, $D_0$ and $\mu$ are parameters of an intrinsic DSD. The number of observed raindrops in a volume is a random variable following a Poisson distribution with the expected value $N_{tv}$ (Chandrasekar and Bringi, 1987; Wong and Chidambaram, 1985). Given a number of observed droplets, i.e. by sampling the Poisson distribution, a simulated distribution of droplets can be obtained by sampling the Gamma probability density function defined by the intrinsic DSD parameters.

Because we need to link intrinsic and observation DSD spaces, the forward model must be applied to a range of DSD parameters. This range should mimic local climatology or cover a wide enough range of DSDs. In this study, observations of DSD parameters collected in Hyytiälä between 2014 and 2024 are used to define this range. The observed distributions of the DSD parameters, namely $D_0$, $\mu$ and $log_{10}(N_w)$ (see Fig. 1) resemble those derived over a five-year period at another location in

https://doi.org/10.5194/egusphere-2026-507
Preprint. Discussion started: 29 January 2026


Finland (Leinonen et al., 2012). Note that a different filtering method is applied in this study. When comparing the cumulative density function (CDF) at these two locations, a CDF of 0.8 is reached at around the same values for the DSD parameters. In Hyytiälä, this corresponds to a $D_0$, $\mu$ and $log_{10}(N_w)$ of 1.1 $\mathrm{mm}$, 10 and $3.8 \times 10^3$ $\mathrm{mm}^{-1}\mathrm{m}^{-3}$, compared to the values reported by Leinonen et al. (2012), which are 1.1 $\mathrm{mm}$, 12 and $3.6 \times 10^3$ $\mathrm{mm}^{-1}\mathrm{m}^{-3}$, respectively.

Differences emerge only in $D_0$ values below 0.7 $\mathrm{mm}$, together with a minor increase in values of $log_{10}(N_w)$. The probability density functions in Fig. 1 are used as inputs into the forward model. To avoid that the intrinsic DSDs are sampled from a climatology containing measurement uncertainties, the distributions are slightly expanded. This also ensures that rarely occurring DSD parameter combinations are included in the simulations. A normal distribution is fitted to $D_0$ and $\mu$ ranging from 0 to about 4 $\mathrm{mm}$ and from -2 to about 60, respectively. For $log_{10}(N_w)$, a uniform distribution is fitted in between the range 2 to 5 $\mathrm{mm}^{-1}\mathrm{m}^{-3}$. Furthermore, physical constraints are established for a reflectivity of $< 55$ $\mathrm{dBZ}$ and rain rate of $< 300$ $\mathrm{mm\,h}^{-1}$ (Chandrasekar and Bringi, 1987). Intrinsic DSDs are formed by drawing a random sample of all three parameters.

The forward model procedure can be described by the following steps:

Step 1 Select intrinsic $D_0$, $\mu$ and $N_w$ by taking a random sample of the observed distributions. Check that the combination of the DSD parameters is reasonable, namely that the reflectivity is less than 55 $\mathrm{dBZ}$ and the rain rate is less than 300 $\mathrm{mm\,h}^{-1}$ (Chandrasekar and Bringi, 1987; Moisseev and Chandrasekar, 2007).

Step 2 Compute expected $N_{tv}$ and sample the Poisson distribution to obtain the number of droplets that will be used to simulated DSD.

Step 3 Using the simulated number of droplets, derive their diameters by sampling a Gamma pdf defined by the intrinsic $D_0$, $\mu$ and $N_w$.

Step 4 Apply filtering to the simulated DSD, i.e. data quality filtering that is applied to the disdrometer observations. Apply small diameter threshold, defined by the disdrometer sensitivity. A Parsivel disdrometer will not record droplets smaller than 0.3-0.4 mm in diameter. To simulate this, we reject simulated DSD values for diameters less than 0.4 mm.

Step 5 Compute DSD parameters from the simulated DSD

Step 6 Repeat Steps 2-5 100 times. We have decided to repeat this calculations 100 times to obtain enough statistics linking the intrinsic DSD and simulated DSD space.

Repeat these steps until you are satisfied that the intrinsic $D_0$, $\mu$ and $N_w$ represent the observed DSD statistics. It should be noted that it is not necessary to reproduce the observed pdf. One can choose to sample a wide enough distributions of $D_0$, $\mu$ and $N_w$ that cover the range of possible DSD parameter values.

The result of the forward model simulations is a set of intrinsic DSDs, each with its corresponding ensemble of simulated DSD parameters, as schematically depicted in Fig. 2a. In our study, the simulated DSD parameter ensemble is 100 times larger than the intrinsic one. Since the parameters of the forward model are selected to represent disdrometer observations, the simulated DSDs mimic disdrometer observations and should include all the uncertainties.

https://doi.org/10.5194/egusphere-2026-507
Preprint. Discussion started: 29 January 2026


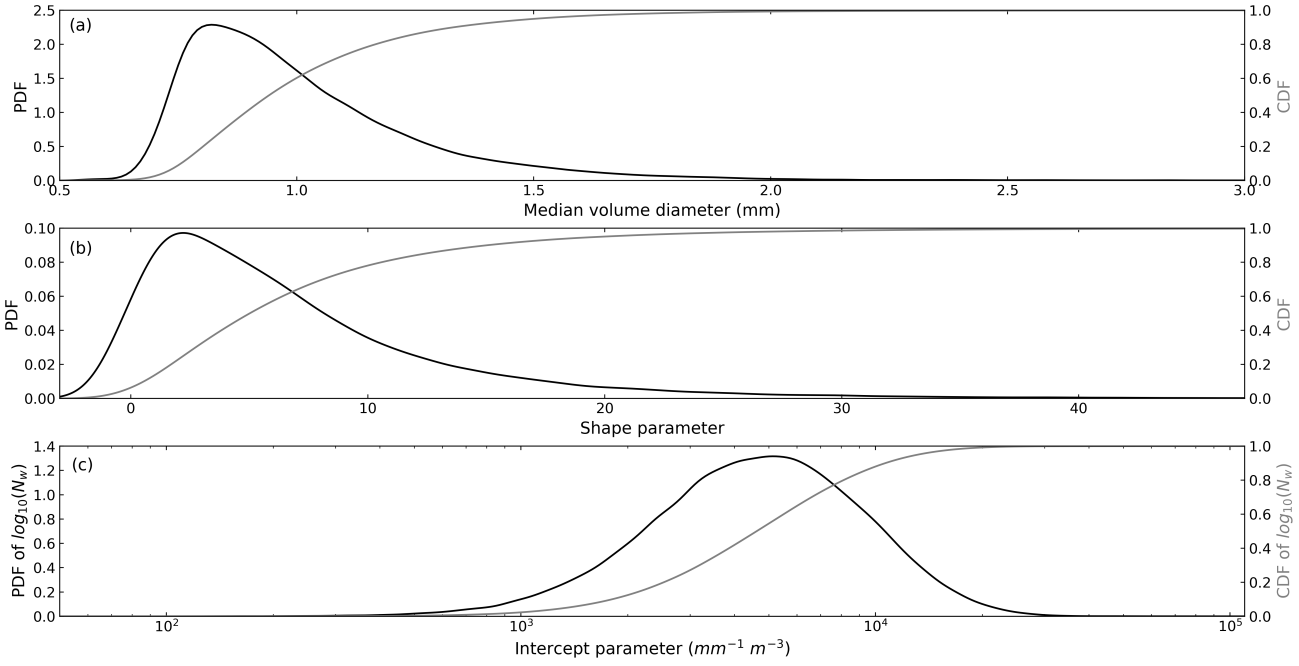


**Figure 1.** The probability density function (PDF) and the cumulative density function (CDF) of (a) the median volume diameter ($D_0$), (b) the shape parameter ($\mu$), and (c) the normalized intercept parameter ($N_w$). Data from Hyytiälä spanning the years 2014 to 2024 are used. Similar as in Fig. 4, 5 and 6 in Leinonen et al. (2012), but with a different filtering method.

### 3.4 Inverse problem; from observations to an ensemble of intrinsic DSDs

The forward model establishes a relationship between an intrinsic DSD and a DSD that mimics observations. The purpose of the inversion is to link an observed DSD with a set of intrinsic DSDs, which given the measurement uncertainty could produce the observation. At the forward modeling stage for every intrinsic DSD, we define a three dimensional, the $D_0$, $\mu$, and $N_w$ space, which is described by the ensemble of corresponding simulated DSD parameters. This space is defined as an ellipsoid, which is characterized by the center, median of the simulated DSD parameters values, and standard deviations corresponding to each DSD parameter that represent axes. Because the DSD parameters vary over a significantly different range of values, the range of DSD parameters are scaled to vary between 0 and 1. The normalization is done by min-max scaling ($\frac{x-x_{min}}{x_{max}-x_{min}}$). The minimum and maximum for each DSD parameter is determined by the minimum and maximum values found in the simulated DSDs for all intrinsic DSDs. This results in a normalized ensemble of simulated DSDs, from which the median and standard deviation are computed. In our case, the minimum and maximum values found for $D_0$, $\mu$, and $N_w$ are 0.48-5.45, -2.59-125.5, and 25.68-$1.07 \times 10^5$, respectively. Since the spread within each ensemble of simulated DSDs is influenced by the number of droplets, the standard deviation is likewise dependent on the droplet count (Fig. 3). To capture this relationship, a second degree polynomial is fitted to describe a relation between the standard deviation and the number of droplets, see Fig. 3.

https://doi.org/10.5194/egusphere-2026-507
Preprint. Discussion started: 29 January 2026


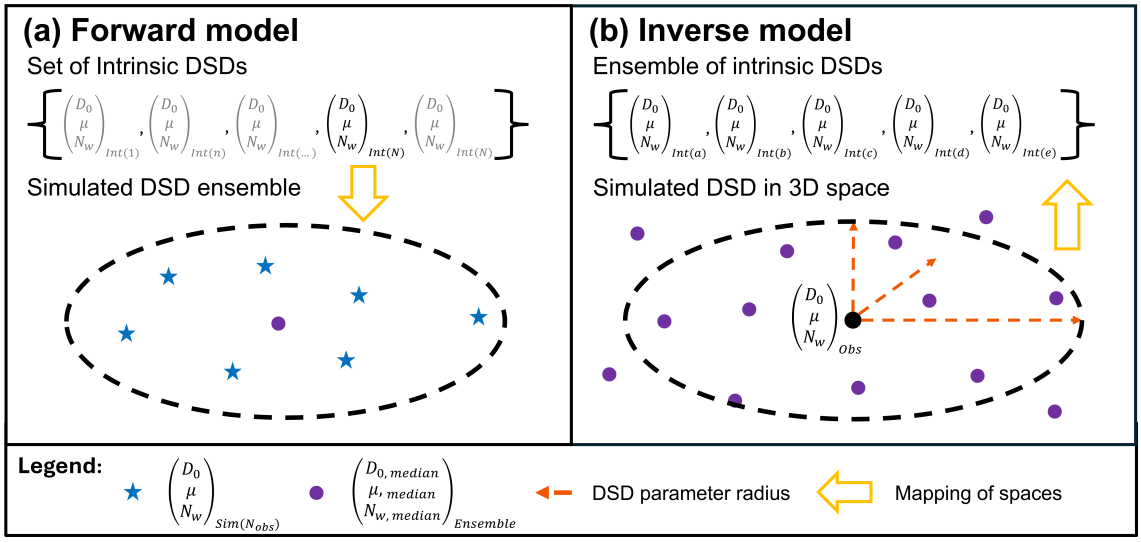


**Figure 2.** Schematic illustrating the steps taking in the forward (a) and inverse (b) models. The forward model relates a single intrinsic DSD to an ensemble of simulated DSDs (blue stars). The inverse model links the disdrometer observed DSD (black dot) to an ensemble of intrinsic DSD via the medians of the simulated ensemble (purple dots). The DSD parameter radius is indicated with orange arrows and the mapping is represented by the gold arrow.

The relations are listed below:

$$\begin{aligned} D_0 &: 1.43\times10^{-3}\,x^2 - 1.02\times10^{-2}\,x + 1.93\times10^{-2} \\ \mu &: \quad 4.19\times10^{-3}\,x^2 - 3.57\times10^{-2}\,x + 7.85\times10^{-2} \\ N_w &: 2.38\times10^{-3}\,x^2 - 1.96\times10^{-2}\,x + 4.17\times10^{-2} \end{aligned} \tag{9}$$

Because each observed DSD contains a specific number of droplets, the relations presented in Eq. (9) provide the radius for each parameter. Together, these radii define an ellipsoid around the observed DSD. We also know how the intrinsic DSD relates to the median of the ensemble of simulated DSDs. When these simulated DSD medians are mapped into the same parameter space as the observations, the ellipsoid will overlap with multiple of the simulated medians. Each of these medians corresponds to an intrinsic DSD, resulting in an ensemble of intrinsic DSDs associated with each observed DSD. This procedure is repeated for every observed DSD, and a single intrinsic DSD can be linked to multiple observations. Because the forward model includes statistical uncertainties, DSD truncation and filtering, this link allows estimation of statistical uncertainties and possible biases of computed DSD parameters and radar variables. Fig. 2b depicts schematically how an observed DSD can be linked to the simulated DSDs and to the corresponding intrinsic DSD variables.

Figure 4 presents an example of an observed DSD, red line, fitted DSD using DSD moments, green line, and estimated DSD using median values of ensembles of intrinsic DSD parameters, blue line. The intrinsic DSD also includes uncertainties of the DSD estimate. It should be noted that these two curves fit the observations well, the main differences appear in the small diameter range, D < 0.5 mm. Because of the disdrometer sensitivity, there are no measurements below 0.3 mm, as

https://doi.org/10.5194/egusphere-2026-507
Preprint. Discussion started: 29 January 2026


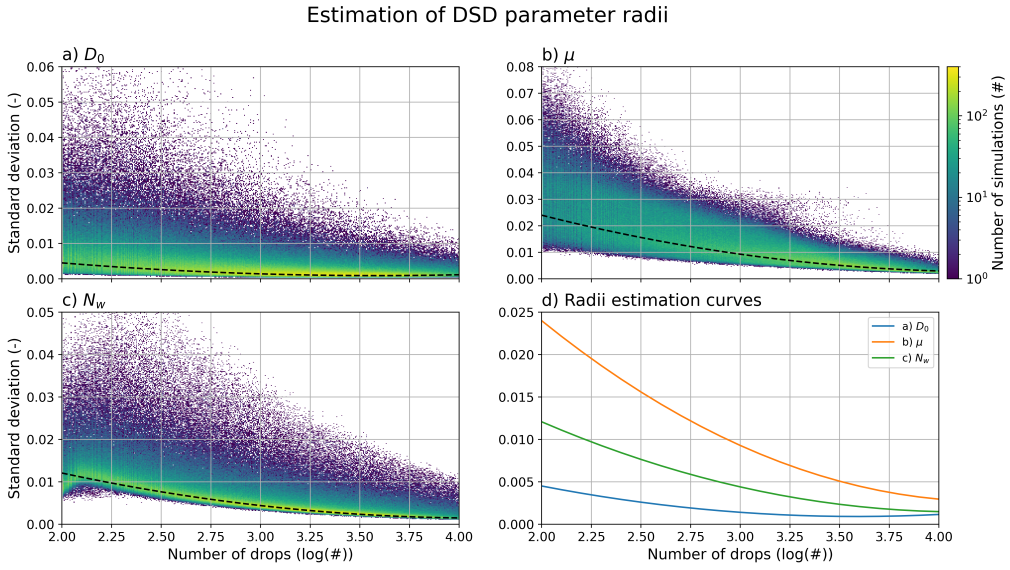


**Figure 3.** Drop size distribution parameter ellipsoid radii estimation for the number of drops in log-scale. Radii estimation is computed from the normalized standard deviations of simulated DSDs for (a) $D_0$, (b) $\mu$, (c) $N_w$. In (a)-(c), the dotted line represents the fitted second degree polynomial and the colors show the number of simulations. The DSD parameters polynomials are shown together in (d), where $D_0$ (blue line), $\mu$ (orange line), and $N_w$ (green line) are displayed.

per manufacturer specifications, see (Moisseev and Chandrasekar, 2007), for example, for discussion on how it would affect DSD parameter estimation. The under sampling of smaller droplets can also be seen in the ensembles of estimated intrinsic DSD parameters. The median volume diameter computed using DSD moments is larger than most intrinsic $D_0$, (4d). Because intrinsic $D_0$ values are smaller and computed reflectivity factor and rainfall rate values, (4b-c), are not too different from the values estimated from the directly fitted DSD, the intrinsic $N_w$ values are somewhat larger (4f). It should also be noted that the estimated intrinsic $\mu$ is smaller than the one directly computed from the observed DSD (4e).

As was shown in (4b-c) the ensembles of reflectivity and rain rates can also be estimated. These estimates are used to compute the associated uncertainties. For measurement stations that are equipped with precipitation gauges, the precipitation rate and accumulation can be used as an additional verification step for the DSD estimates. Because the uncertainties associated with the ensemble of rain rate are correlated, the standard deviation of the accumulated precipitation can not be directly added over time. Therefore, the propagation of uncertainty is calculated by $\sigma^2 = a \sum^x a^T$, where $a$ is a row vector and $\sum^x$ is the variance-covariance matrix (Mardia et al., 1979). Estimation of the radome attenuation is based on a comparison of computed and measured reflectivity factors. If the difference is larger than the expected uncertainty, radome attenuation is identified and computed. For the rain path attenuation, the specific attenuation is computed form the disdrometer observations. Under ideal conditions, the specific attenuation should be equal to the slope of the reflectivity profile.

https://doi.org/10.5194/egusphere-2026-507
Preprint. Discussion started: 29 January 2026


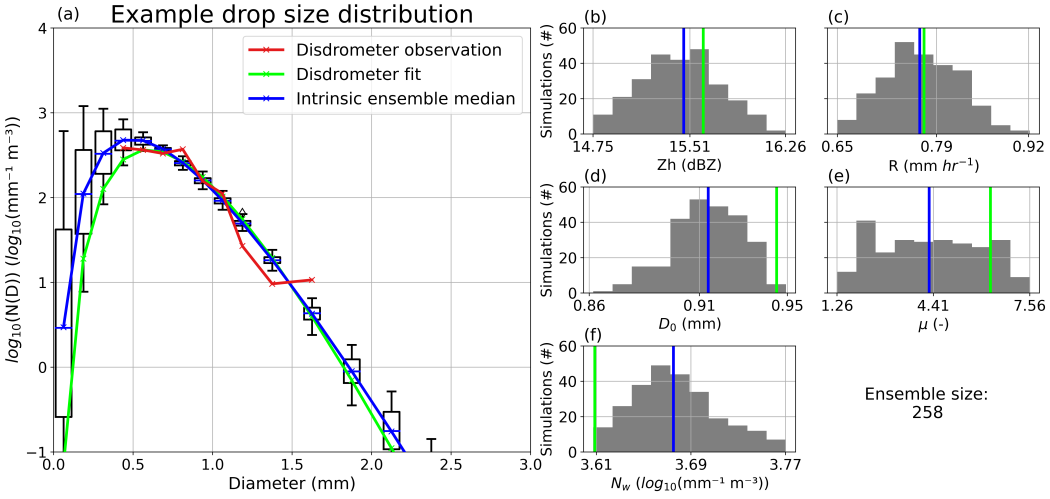


**Figure 4.** An example of an observed DSD (red line) with its fitted DSD using DSD moments (green line) and corresponding ensemble of intrinsic DSDs (black boxes) and ensemble median (blue line) in (a). Histograms (b)-(f) show the ensemble of intrinsic DSDs (gray) with its ensemble median (blue line) and the DSD fit using DSD moments (green line). From (b) to (f) are respectively computed reflectivity, rain rate, $D_0$, $\mu$, and $N_w$. The ensemble size of intrinsic DSDs corresponding to the observed DSD is displayed on the bottom right.

## 4 Results

Two rain events recorded on 26 May 2022 and 28-29 July 2023 are presented to illustrate the proposed method, see Fig. 5 and Fig. 6. The main difference between these events is the radome attenuation. On 26 May 2022 the radome attenuation is negligible, while during the event on 28-29 July 2023 the radome attenuation approaches 10 dB. In both cases rain lasted for extended periods of time.

On 26 May 2022 the stratiform precipitation started around 1 UTC and continued past 20 UTC, see Fig. 5. During this event the largest fraction of precipitation accumulation occurred between 5 and 12 UTC. Figure 5b-c show DSD based computations as compared to radar and precipitation gauge observations. For the radar reflectivity factor comparison, radar observations at the $3^{rd}$ range gate (153.3 m) are compared to disdrometer based estimates. Both estimates based on direct disdrometer observations and intrinsic ensembles are shown. The proposed approach allows estimation of the uncertainty range as depicted by shading and is expressed as the range corresponding to $\pm 1$ and $\pm 2$ standard deviations. For the radar reflectivity factor the uncertainty range is relatively small with a standard deviation of around 0.3 dB. For the precipitation accumulation the uncertainties accumulate and can be seen in the increasing range as shown by the red shaded area.

The event on 28-29 July started with a brief period of convective precipitation on the $28^{th}$ around 14 UTC, which was followed by an extended period of stratiform precipitation, with intermittent moderate rainfall, lasting until about 13 UTC on the $29^{th}$, see Fig. 6. The stratiform precipitation can be divided in two phases: approximately two thirds of the accumulated stratiform precipitation occurred on the $28^{th}$ between 14 UTC and midnight, while the remaining one third occurred from

https://doi.org/10.5194/egusphere-2026-507
Preprint. Discussion started: 29 January 2026


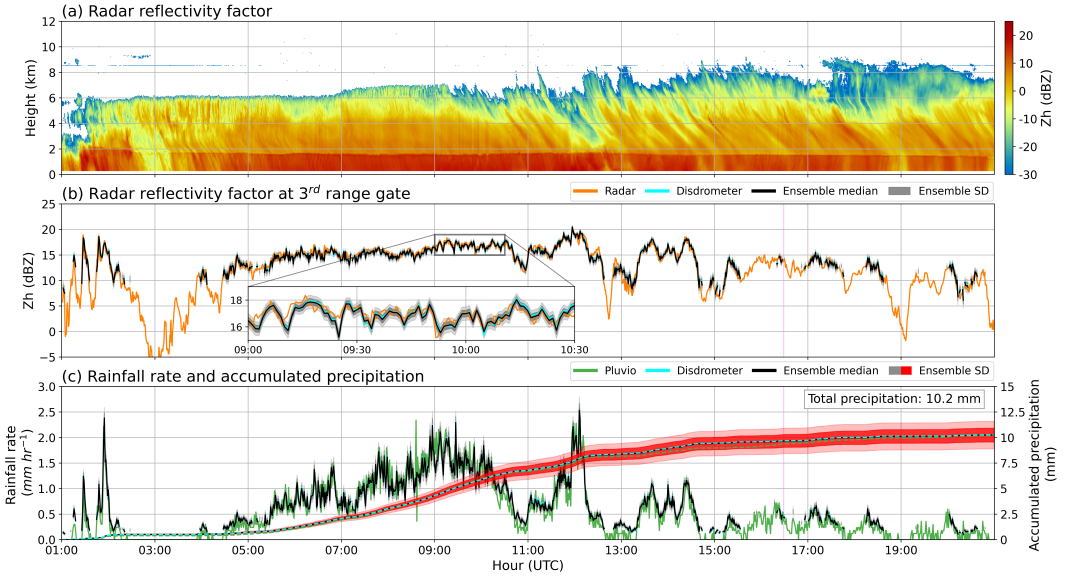


**Figure 5.** Time-height plot of (a) HYDRA-W radar reflectivity factor. Time series of the (b) radar reflectivity factor at $3^{rd}$ range gate and of (c) rainfall rate (left side) and accumulated precipitation (right side). The time is set to capture the event between 1 and 20 UTC. In (b), the reflectivity factor is shown together with the Parsivel computed reflectivity (cyan line) and the ensemble of intrinsic DSDs median (black line) and standard deviation (SD) ($\pm 1\sigma$ darker shading and $\pm 2\sigma$ lighter shading). (c) displays the rainfall rate and the accumulated precipitation with similar color coding as in (b), but with Pluvio (green line) instead of radar. The total precipitation of the event is shown at the top of (c). The inset axis in (b) provides a detailed look between 9 and 10:30 UTC. The method could not be applied at the times indicated by the magenta vertical lines in (b) and (c).

midnight till 13 UTC on the $29^{th}$ (Fig. 6c). Uncertainty in the radar reflectivity factor during this event is comparable to that observed for the 26 May event.

To allow a comparison of computed and observed radar variables, data need to be corrected for a potential time lag. This time delay is identified as the lag where a maximum of the cross correlation between radar measured and disdrometer derived reflectivity factor values is observed. For both events, this lag was found to be about one minute.

### 4.1 Radome attenuation

An estimate of the wet radome attenuation is obtained by computing the difference between radar reflectivity at the lowest usable range gate ($3^{rd}$ gate) and the "median intrinsic reflectivity". This is illustrated for an event with minimal radome attenuation and one with a degraded radome resulting in strong radome attenuation. The selection of events is performed to ensure that there is a prolonged period of continuous rainfall. An event with minimal radome attenuation was observed on the $26^{th}$ of May 2022 (Fig. 5). The light rain (<2.5 $\mathrm{mm\,hr^{-1}}$) starts at 05:21 UTC and ends at 12:38 UTC (Fig. 5c, left axis). Before the start of the continuous rain, some light drizzle occurred. To assess the effect of the continuous rain on the

https://doi.org/10.5194/egusphere-2026-507
Preprint. Discussion started: 29 January 2026


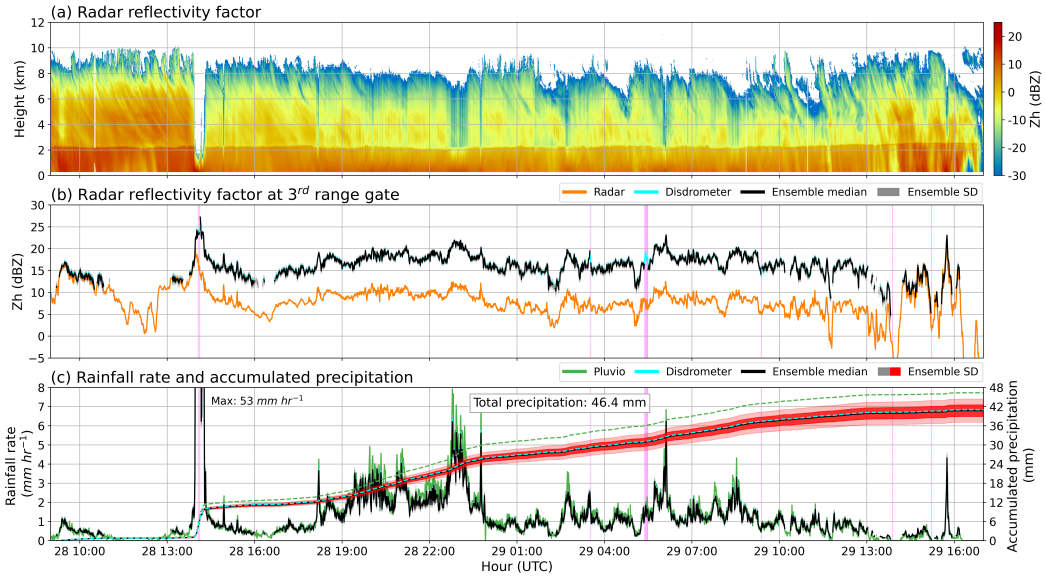


**Figure 6.** Same as in Fig. 5, but for the event on July 28-29 2023 between 9 and 17 UTC.

radome, we compare the radar (in orange) and intrinsic (in black) reflectivity values (Fig. 5b). These two lines match almost exactly, indicating that the radome attenuation is negligible. The computed radome attenuation is shown in Fig. 7c (right side). Throughout the rain event, the radome attenuation did not exceed 1 dB for 82% of the time.

In contrast, the second event demonstrates significant radome attenuation, as can be seen in Fig. 6. The rain starts on the $28^{th}$ at 13:46 UTC and ends on the $29^{th}$ at 13:02 UTC. At the beginning of the event, heavy rainfall (reaching 53 $\mathrm{mm\,hr^{-1}}$) is observed, which saturated the radome almost instantly causing strong radome attenuation (Fig. 6c). This strong attenuation is also visible in Fig. 6a, as indicated by a sharp drop in reflectivity. Following the heavy rain, there was a prolonged period of light to moderate precipitation. By comparing the radar reflectivity (in orange) with the intrinsic reflectivity (in black) shown in Fig. 6b, it becomes apparent that the radome became wet at the point where the two lines begin to diverge. This difference is maintained throughout the event. The resulting radar attenuation is shown in Fig. 8c (right axis). Prior to the rain shower, the radome attenuation is minimal, but it increases significantly to a range between 7 and 8 dB once the heavy rain begins. Once the intense precipitation ceased, the rain rate diminishes, enabling the radome to gradually dry, which is reflected by a decline in radome correction. With the return of moderate rain, attenuation values increase gradually to approximately 10 dB. At the end of the rainfall, the radome dried quickly, and the attenuation values returned to levels observed at the beginning of this precipitation event. Similar radome attenuation values around 10 dB at the W-band wavelength have been reported by Myagkov et al. (2020) and Hogan et al. (2003).

It should be noted that during the second event, there is also a notable difference in observations of precipitation accumulation. The weighing gauge measures about 47 mm of total precipitation accumulation during the event and disdrometer derived accumulation is only 42 mm. This difference exceeds expected uncertainty of disdrometer observations.

https://doi.org/10.5194/egusphere-2026-507
Preprint. Discussion started: 29 January 2026


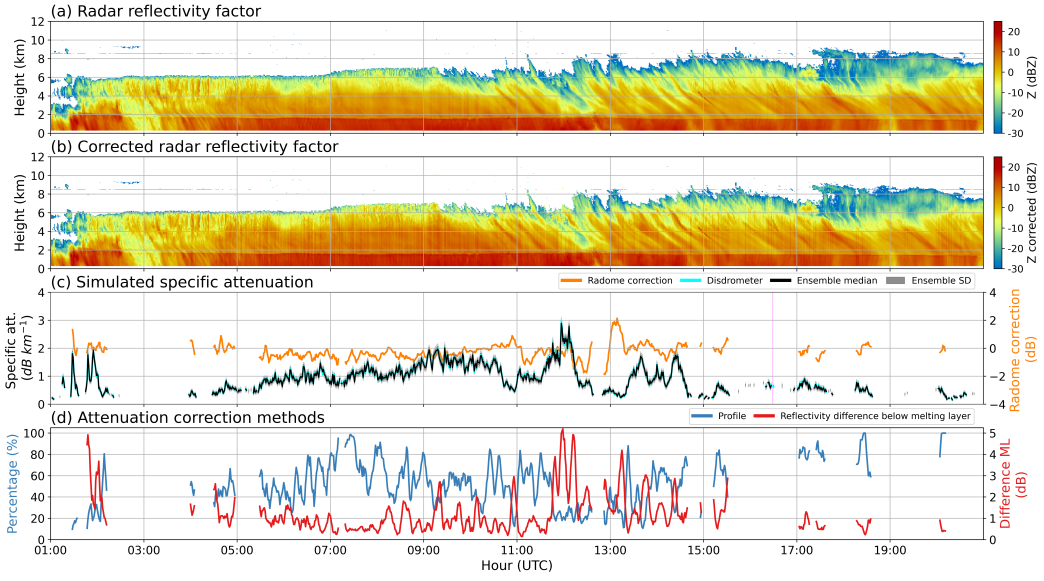


**Figure 7.** Time-height plot of HYDRA-W (a) uncorrected and (b) corrected radar reflectivity factor. Time series of the (c) specific attenuation observed by disdrometer (cyan line) and median (black line) and standard deviation (SD) ($\pm 1\sigma$ darker shading and $\pm 2\sigma$ lighter shading) of the ensemble of intrinsic DSDs, left side, and magnitude of the radome correction applied to the reflectivity factor (orange line), right side. In (d), the two methods used to verify whether attenuation correction is applicable are presented. On the left, the percentage of slope falling within $\pm 2$ standard deviation (blue line), while on the right, the difference below the melting layer (red line) is shown. Both lines are averaged over 5 minute instead of the 1 minute used in the method. The time span is identical to that in Fig. 5.

### 4.2 Specific attenuation

In addition to the radome attenuation, the rain path attenuation can be computed if certain conditions are met. If the changes in reflectivity values with height in rain are mainly caused by attenuation, the slope of the reflectivity profile is equal to the specific attenuation. Using disdrometer observations, specific attenuation can be computed and compared to radar observations. For each DSD observation specific attenuation is computed from the intrinsic ensemble, which takes into account the uncertainties arising from the relatively small sampling volume. The median of the ensemble defines the expected value of the specific attenuation. Additionally, the standard deviation of the computed specific attenuation values is used as uncertainty range.

The attenuation correction consists of two main steps. After the radome attenuation is corrected, we compute the expected profile of the radar reflectivity. The profile spans from the third range gate up to the bottom of the melting layer. The melting layer boundaries are estimated using linear depolarization ratio observations (Li and Moisseev, 2020). The expected profile of the reflectivity expressed in dBZ units is modeled as a linear function with a slope equal to the specific attenuation. In addition to the expected reflectivity profile, the confidence region is also computed. At the second step, the computed and observed reflectivity profiles are compared to assess if the attenuation correction can be applied.

https://doi.org/10.5194/egusphere-2026-507
Preprint. Discussion started: 29 January 2026


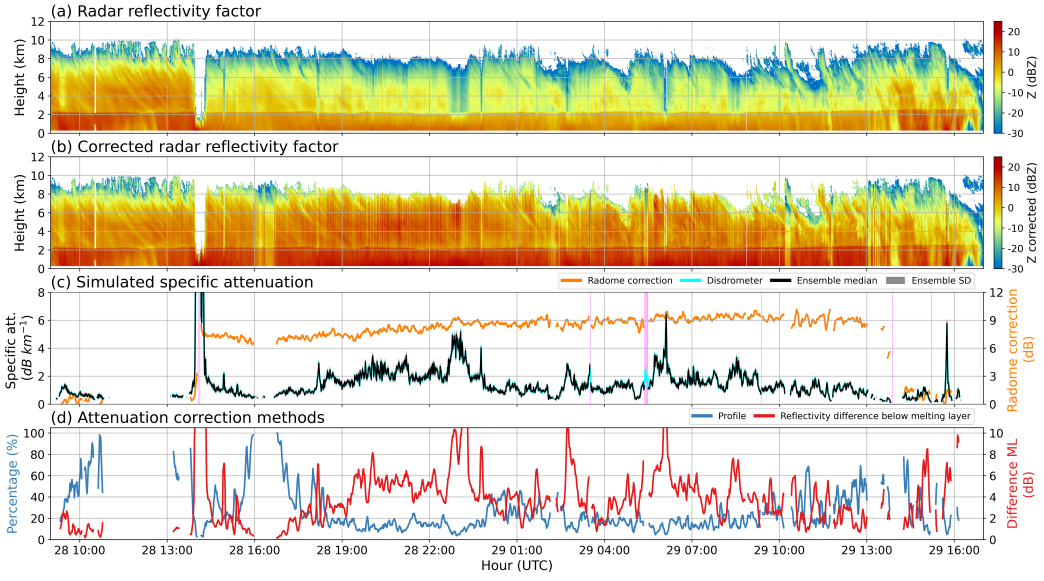


**Figure 8.** Same as in Fig. 8, but for the event on 28-29 July 2023 between 9 and 17 UTC.

There are several reasons that can cause differences between observed and derived profiles. The radio waves are attenuated by the vertical precipitation column. Given that we are observing DSD properties at the ground, we assume that the whole column is characterized by these observations. Spatial and temporal variations in the precipitation intensity combined with wind shear could results in fall streaks which would affect representativeness of surface observations. Additionally, changes in precipitation intensity due to evaporation or collision-coalescence growth are also not captured by disdrometer observations.

In Fig. 9 the proposed attenuation correction method is illustrated based on observations collected on 26 May 2022. The figure shows observations of radar reflectivity factor and ceilometer attenuated backscatter. During this event, the specific attenuation varies between 0.5 to 3.0 $\mathrm{dB\,km^{-1}}$ see Fig. 7c (left axis). Four profiles observed at 0605, 0850 1030 and 1400 UTC were selected for a more detailed comparison of the observed, black line, and modeled, green dashed line, reflectivity profiles. The reflectivity factor values computed from the disdrometer observations are shown by the error bars. The median reflectivity value matches radar observations at the third gate. The uncertainty range for the specific attenuation are depicted by red and blue dashed lines, corresponding to $\pm 2$ standard deviation. Because reflectivity and specific attenuation values are correlated, higher reflectivity values correspond to higher specific attenuation values. This effect can be seen in the difference of the slopes of the modeled profiles for the selected times. Also slopes of the red and blue dashed lines, which correspond to lower and higher ranges of uncertainty, are different, because they originate from the upper and lower bounds of the estimated reflectivity values.

We propose two methods to assess whether the attenuation correction can be applied. The first method checks if the observed reflectivity profile lies within the $\pm 2$ standard deviation as estimated from DSD observations. If more than 75 % of the observed reflectivity profile lies between lower and upper uncertainty bounds, the two profiles are considered to be similar enough to

https://doi.org/10.5194/egusphere-2026-507
Preprint. Discussion started: 29 January 2026


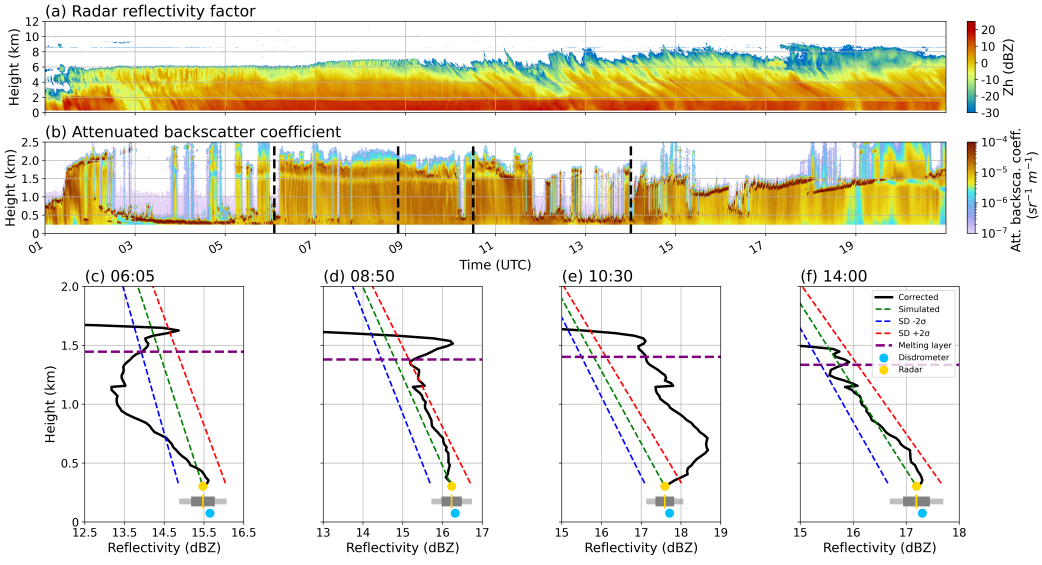


**Figure 9.** Time-height plot of (a) HYDRA-W radar reflectivity factor and (b) ceilometer attenuated backscatter. The time span is identical to that in Fig. 5. Reflectivity profiles (c)-(f) illustrate the observations at 0605, 0850 1030 and 1400 UTC, respectively. The radome corrected reflectivity profile (black) is shown together with the ensemble of intrinsic DSDs, including the median (green dotted line) and the upper and lower $\pm 2$ standard deviation bounds (red and blue dotted lines). The ensemble spread is additionally represented as error bars indicating the median (gold) and $\pm 2$ standard deviations (SD) ($\pm 1\sigma$ darker shading and $\pm 2\sigma$ lighter shading). The melting layer is indicated by the horizontal purple dotted line. Cyan and gold dots denote the reflectivity observed by the disdrometer and at the third radar gate, respectively.

apply the attenuation correction. The 75 % threshold is an ad hoc criterion selected to be sufficiently strict without being too restrictive. As can be seen in Fig. 9, only two of the selected profiles would satisfy this criterion. The difference can be attributed to the seeder-feeder process, where raindrops are growing by collision-coalescence in the embedded cloud layers. The presence of the embedded cloud layers is evident in the attenuated backscatter measurements. Fig. 7d and 8d present the overlap percentage of observed and modeled reflectivity profiles for the two events. As can be seen, for these two analyzed events only for a small fractions of observations the overlap percentage is high enough. A second, less restrictive criterion is to compare projected and observed reflectivity values just below the melting layer. If the difference is less than 1 dB, than the attenuation correction can be applied. In Fig. 7d and 8d the reflectivity difference is plotted. It is less than 1 dB for a large fraction of the 26 May 2022 event. For the 28-29 July 2023 case, even this less restrictive criterion fails for a large fraction of the event. During 28-29 July 2023 rain event there was a persistent low-level cloud, with a cloud base below 1 km. Because of the cloud the surface precipitation observations are affected by the seeder-feeder process and not representative of the whole rain column. The melting layer was at about 2 km for this case.

As part of the Cloudnet processing chain (Tukiainen et al., 2020), a rain-attenuation correction following (Crane, 1980) has been applied since September 2024. This correction was implemented in Cloudnetpy version 1.66 (Tukiainen et al., 2024). It

https://doi.org/10.5194/egusphere-2026-507
Preprint. Discussion started: 29 January 2026


is based on a parameterization that relates the rain rate, derived from disdrometer measurements, to the specific attenuation, as presented in (Crane, 1980). The limitations of this method are essentially the same as for the approach presented in this paper. It is assumed that surface-based observations of rainfall microphysical properties are representative of the entire atmospheric column.

Prior to Cloudnetpy version 1.66 (Tukiainen et al., 2024), no attenuation correction was applied, and consequently, ice water content (IWC) retrievals were not performed in conditions affected by uncompensated rain attenuation. Figures 10a and 11a show the IWC retrieval status reported for the two case studies before the introduction of the attenuation correction in version 1.66. After applying the second criterion that determines whether the attenuation correction can be reliably used, the IWC retrieval status was revised, as illustrated in Figures 10b and 11b. In addition, the presence of embedded liquid cloud layers is explicitly indicated. These layers are flagged starting from the detected cloud base up to the base of the melting layer, under the assumption that lower cloud layers exert a stronger influence on the attenuation because in such case the observed DSD is only representative of a limited fraction of a vertical profile. This hypothesis is supported by observations from these two events. It can be seen in the figures that the reflectivity matching criterion fails in cases where clouds are present. In some cases where the cloud layers appear closer to the melting layer the attenuation correction can still be applied.

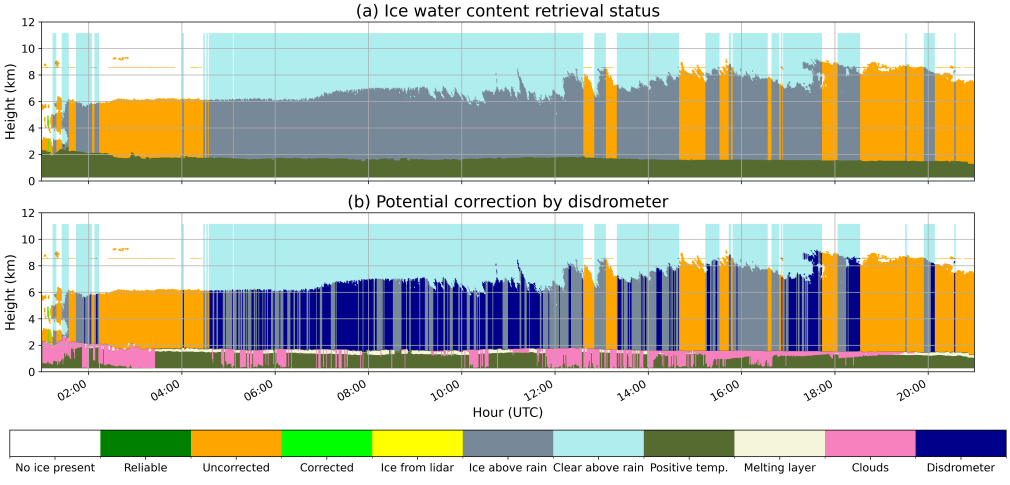


**Figure 10.** Time-height plot of the ice water content retrieval status (a) without attenuation correction and (b) after applying attenuation correction using the second method. The time span is identical to that in Fig. 5. Periods with clouds are indicated in magenta, and profiles where attenuation correction is applicable are marked in blue.

https://doi.org/10.5194/egusphere-2026-507
Preprint. Discussion started: 29 January 2026


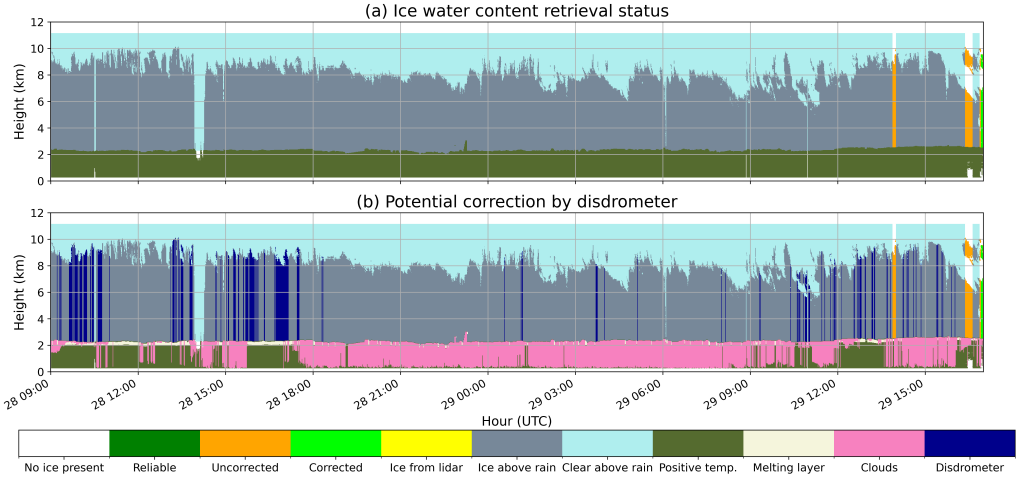


**Figure 11.** Same as in Fig. 10, but for the event on 28-29 July 2023 between 9 and 17 UTC.

## 5 Conclusions

In this study, the uncertainties associated with the application of radome attenuation and rain path attenuation corrections based on disdrometer observations are investigated. It is shown that statistical uncertainties arising from sampling of the drop size distribution (DSD) with disdrometers such as the Parsivel can be quantitatively characterized. This uncertainty quantification framework enables the evaluation of radome attenuation, as attenuation events can be identified when the discrepancy between measured radar reflectivity and DSD derived radar reflectivity exceeds the corresponding uncertainty range. In addition to comparing observed and computed radar reflectivity, precipitation accumulations recorded by a weighing gauge and a disdrometer were analyzed. For one of the events, the observed discrepancy could not be explained by statistical sampling uncertainty alone.

Because radome attenuation can become substantial during intense precipitation, even for weather radars equipped with radome blowers, radar calibration monitoring procedures that rely on disdrometer data should explicitly account for this effect. The use of disdrometer observations for rain path attenuation correction is also examined. Two criteria are introduced to assess whether the disdrometer measurements are representative of the overlying rain column and therefore suitable for use in attenuation correction. Analysis of selected case studies indicates that embedded cloud layers pose a significant challenge for the applicability and reliability of this approach. These findings highlight the need to evaluate the attenuation correction procedures implemented in Cloudnetpy and to better understand their limitations.

*Code and data availability.* The data used in this study are generated by the Aerosol, Clouds and Trace Gases Research Infrastructure (ACTRIS) and are available from the ACTRIS Data Centre using the following links: https://doi.org/10.60656/1fe3a02ef09b419d,

https://doi.org/10.5194/egusphere-2026-507
Preprint. Discussion started: 29 January 2026


https://doi.org/10.60656/d25b530af3d04367 and https://doi.org/10.60656/8d288976932d417e. The code is available on GitHub at https://github.com/berndmom/ERAC.

*Author contributions.* BM and DM have conceptualized the study. BM developed the methodology with input from DM. BM has implemented the methodology, processed the data, and performed the analysis. Both authors have contributed to writing of the manuscript.

*Competing interests.* There are no competing interests

*Acknowledgements.* We acknowledge ACTRIS and Finnish Meteorological Institute for providing the data set which is available for download from https://cloudnet.fmi.fi. We acknowledge ECMWF for providing IFS model data.

This work was supported by funding from Horizon Europe programme under Grant Agreement No 101137680 via project CERTAINTY (Cloud-aERosol inTeractions & their impActs IN The earth sYstem) and Research Council of Finland (decision 369601).

https://doi.org/10.5194/egusphere-2026-507
Preprint. Discussion started: 29 January 2026


## References

Atlas, D. and Ulbrich, C. W.: Path- and Area-Integrated Rainfall Measurement by Microwave Attenuation in the 1–3 cm Band, Journal of Applied Meteorology, 16, 1322–1331, https://doi.org/10.1175/1520-0450(1977)016<1322:PAAIRM>2.0.CO;2, 1977.

Atlas, D., Srivastava, R. C., and Sekhon, R. S.: Doppler radar characteristics of precipitation at vertical incidence, Reviews of Geophysics, 11, 1–35, https://doi.org/10.1029/RG011i001p00001, _eprint: https://onlinelibrary.wiley.com/doi/pdf/10.1029/RG011i001p00001, 1973.

Bringi, V. N. and Chandrasekar, V.: Polarimetric Doppler Weather Radar: Principles and Applications, Cambridge University Press, Cambridge, ISBN 978-0-521-62384-1, https://doi.org/10.1017/CBO9780511541094, 2001.

Carey, L. D. and Petersen, W. A.: Sensitivity of C-Band Polarimetric Radar–Based Drop Size Estimates to Maximum Diameter, Journal of Applied Meteorology and Climatology, 54, 1352–1371, https://doi.org/10.1175/JAMC-D-14-0079.1, 2015.

Chandrasekar, V. and Bringi, V. N.: Simulation of Radar Reflectivity and Surface Measurements of Rainfall, Journal of Atmospheric and Oceanic Technology, 4, 464 – 478, https://doi.org/10.1175/1520-0426(1987)004<0464:SORRAS>2.0.CO;2, 1987.

Crane, R.: Prediction of Attenuation by Rain, IEEE Transactions on Communications, 28, 1717–1733, https://doi.org/10.1109/TCOM.1980.1094844, 1980.

Deng, M., Giangrande, S. E., Jensen, M. P., Johnson, K., Williams, C. R., Comstock, J. M., Feng, Y.-C., Matthews, A., Lindenmaier, I. A., Wendler, T. G., Rocque, M., Zhou, A., Zhu, Z., Luke, E., and Wang, D.: Wet-Radome Attenuation in ARM Cloud Radars and Its Utilization in Radar Calibration Using Disdrometer Measurements, EGUsphere, pp. 1–42, https://doi.org/10.5194/egusphere-2024-2615, publisher: Copernicus GmbH, 2024.

Giangrande, S. E., Wang, D., Bartholomew, M. J., Jensen, M. P., Mechem, D. B., Hardin, J. C., and Wood, R.: Midlatitude Oceanic Cloud and Precipitation Properties as Sampled by the ARM Eastern North Atlantic Observatory, Journal of Geophysical Research: Atmospheres, 124, 4741–4760, https://doi.org/10.1029/2018JD029667, _eprint: https://onlinelibrary.wiley.com/doi/pdf/10.1029/2018JD029667, 2019.

Gorgucci, E., Bechini, R., Baldini, L., Cremonini, R., and Chandrasekar, V.: The Influence of Antenna Radome on Weather Radar Calibration and Its Real-Time Assessment, Journal of Atmospheric and Oceanic Technology, https://doi.org/10.1175/JTECH-D-12-00071.1, 2013.

Hari, P. and Kulmala, M.: Station for Measuring Ecosystem–Atmosphere Relations (SMEAR II), Boreal Environment Research, 10, 315–322, 2005.

Hitschfeld, W. and Bordan, J.: ERRORS INHERENT IN THE RADAR MEASUREMENT OF RAINFALL AT ATTENUATING WAVELENGTHS, Journal of the Atmospheric Sciences, https://journals.ametsoc.org/view/journals/atsc/11/1/1520-0469_1954_011_0058_eiitrm_2_0_co_2.xml, 1954.

Hogan, R. J. and O'Connor, E. J.: Facilitating cloud radar and lidar algorithms: the Cloudnet Instrument Synergy/Target Categorization product., https://www.met.reading.ac.uk/~swrhgnrj/publications/categorization.pdf, 2004.

Hogan, R. J., Bouniol, D., Ladd, D. N., O'Connor, E. J., and Illingworth, A. J.: Absolute Calibration of 94/95-GHz Radars Using Rain, Journal of Atmospheric and Oceanic Technology, https://journals.ametsoc.org/view/journals/atot/20/4/1520-0426_2003_20_572_acogru_2_0_co_2.xml, 2003.

Hogan, R. J., Illingworth, A. J., O'Connor, E. J., Bouniol, D., Brook, M. E., Delanoë, J., Donovan, D. P., Eastment, J. D., Gaussiat, N., Goddard, J. W. F., Haeffelin, M., Baltink, H. K., Krasnov, O. A., Pelon, J., Piriou, J.-M., Protat, A., Russchenberg, H. W. J., Seifert, A., Tompkins, A. M., Zadelhoff, G.-J. v., Vinit, F., Westbrook, C., Willén, U., Wilson, D. R., and Wrench, C. L.: Cloudnet: Evaluation of model clouds using ground-based observations, Proceedings of the ECMWF Workshop on Parametrization of clouds in large-scale models, Reading, UK, 2006a.

https://doi.org/10.5194/egusphere-2026-507
Preprint. Discussion started: 29 January 2026


Hogan, R. J., Mittermaier, M. P., and Illingworth, A. J.: The Retrieval of Ice Water Content from Radar Reflectivity Factor and Temperature and Its Use in Evaluating a Mesoscale Model, Journal of Applied Meteorology and Climatology, https://doi.org/10.1175/JAM2340.1, 2006b.

Illingworth, A. J. and Blackman, T. M.: The Need to Represent Raindrop Size Spectra as Normalized Gamma Distributions for the Interpretation of Polarization Radar Observations, Journal of Applied Meteorology and Climatology, https://journals.ametsoc.org/view/journals/apme/41/3/1520-0450_2002_041_0286_tntrrs_2.0.co_2.xml, 2002.

Illingworth, A. J., Hogan, R. J., O'Connor, E. J., Bouniol, D., Brooks, M. E., Delanoé, J., Donovan, D. P., Eastment, J. D., Gaussiat, N., Goddard, J. W. F., Haeffelin, M., Baltink, H. K., Krasnov, O. A., Pelon, J., Piriou, J.-M., Protat, A., Russchenberg, H. W. J., Seifert, A., Tompkins, A. M., Zadelhoff, G.-J. v., Vinit, F., Willén, U., Wilson, D. R., and Wrench, C. L.: Cloudnet, Bulletin of the American Meteorological Society, https://doi.org/10.1175/BAMS-88-6-883, 2007.

Kollias, P., Puigdomènech Treserras, B., and Protat, A.: Calibration of the 2007–2017 record of Atmospheric Radiation Measurements cloud radar observations using CloudSat, Atmospheric Measurement Techniques, 12, 4949–4964, https://doi.org/10.5194/amt-12-4949-2019, publisher: Copernicus GmbH, 2019.

Kurri, M. and Huuskonen, A.: Measurements of the Transmission Loss of a Radome at Different Rain Intensities, Journal of Atmospheric and Oceanic Technology, https://doi.org/10.1175/2008JTECHA1056.1, 2008.

Küchler, N., Kneifel, S., Löhnert, U., Kollias, P., Czekala, H., and Rose, T.: A W-Band Radar–Radiometer System for Accurate and Continuous Monitoring of Clouds and Precipitation, Journal of Atmospheric and Oceanic Technology, https://doi.org/10.1175/JTECH-D-17-0019.1, 2017.

Lamb, D. and Verlinde, J.: Physics and Chemistry of Clouds, Cambridge University Press, New York, ISBN 978-0-521-89910-9, 2011.

Lamer, K., Oue, M., Battaglia, A., Roy, R. J., Cooper, K. B., Dhillon, R., and Kollias, P.: Multifrequency radar observations of clouds and precipitation including the G-band, Atmospheric Measurement Techniques, 14, 3615–3629, https://doi.org/10.5194/amt-14-3615-2021, publisher: Copernicus GmbH, 2021.

L'Ecuyer, T. S. and Stephens, G. L.: An Estimation-Based Precipitation Retrieval Algorithm for Attenuating Radars, Journal of Applied Meteorology and Climatology, https://journals.ametsoc.org/view/journals/apme/41/3/1520-0450_2002_041_0272_aebpra_2.0.co_2.xml, 2002.

Leinonen, J.: High-level interface to T-matrix scattering calculations: architecture, capabilities and limitations, Optics Express, 22, 1655–1660, https://doi.org/10.1364/OE.22.001655, publisher: Optica Publishing Group, 2014.

Leinonen, J., Moisseev, D., Leskinen, M., and Petersen, W. A.: A Climatology of Disdrometer Measurements of Rainfall in Finland over Five Years with Implications for Global Radar Observations, Journal of Applied Meteorology and Climatology, https://doi.org/10.1175/JAMC-D-11-056.1, 2012.

Lhermitte, R.: Attenuation and Scattering of Millimeter Wavelength Radiation by Clouds and Precipitation, Journal of Atmospheric and Oceanic Technology, https://journals.ametsoc.org/view/journals/atot/7/3/1520-0426_1990_007_0464_aasomw_2_0_co_2.xml, 1990.

Li, H. and Moisseev, D.: Melting Layer Attenuation at Ka- and W-Bands as Derived From Multifrequency Radar Doppler Spectra Observations, Journal of Geophysical Research: Atmospheres, 124, 9520–9533, https://doi.org/10.1029/2019JD030316, _eprint: https://onlinelibrary.wiley.com/doi/pdf/10.1029/2019JD030316, 2019.

Li, H. and Moisseev, D.: Two Layers of Melting Ice Particles Within a Single Radar Bright Band: Interpretation and Implications, Geophysical Research Letters, 47, e2020GL087 499, https://doi.org/10.1029/2020GL087499, 2020.

https://doi.org/10.5194/egusphere-2026-507
Preprint. Discussion started: 29 January 2026


Löffler-Mang, M. and Joss, J.: An Optical Disdrometer for Measuring Size and Velocity of Hydrometeors, Journal of Atmospheric and Oceanic Technology, https://journals.ametsoc.org/view/journals/atot/17/2/1520-0426_2000_017_0130_aodfms_2_0_co_2.xml, 2000.

Mardia, K. V., Kent, J. T., and Bibby, J. M.: Multivariate Analysis, Academic Press, London, 1979.

Matrosov, S. Y.: Potential for attenuation-based estimations of rainfall rate from CloudSat, Geophysical Research Letters, 34, https://doi.org/10.1029/2006GL029161, _eprint: https://onlinelibrary.wiley.com/doi/pdf/10.1029/2006GL029161, 2007.

Matrosov, S. Y.: Assessment of Radar Signal Attenuation Caused by the Melting Hydrometeor Layer, IEEE Transactions on Geoscience and Remote Sensing, 46, 1039–1047, https://doi.org/10.1109/TGRS.2008.915757, conference Name: IEEE Transactions on Geoscience and Remote Sensing, 2008.

Mishchenko, M. I. and Travis, L. D.: T-matrix computations of light scattering by large spheroidal particles, Optics Communications, 109, 16–21, https://doi.org/10.1016/0030-4018(94)90731-5, 1994.

Mishchenko, M. I., Travis, L. D., and Macke, A.: Scattering of light by polydisperse, randomly oriented, finite circular cylinders, Applied Optics, 35, 4927–4940, https://doi.org/10.1364/AO.35.004927, publisher: Optica Publishing Group, 1996.

Moisseev, D. and Petäjä, T.: Custom collection of disdrometer, and weather station data from Hyytiälä between 1 Jan 2014 and 31 Dec 2024, https://doi.org/10.60656/8d288976932d417e, 2025.

Moisseev, D., O'Connor, E., and Petäjä, T.: Custom collection of categorize, classification, disdrometer, ice water content, and weather station data from Hyytiälä on 26 May 2022, https://doi.org/10.60656/1fe3a02ef09b419d, 2025a.

Moisseev, D., O'Connor, E., and Petäjä, T.: Custom collection of categorize, classification, disdrometer, ice water content, and weather station data from Hyytiälä between 28 and 29 Jul 2023, https://doi.org/10.60656/d25b530af3d04367, 2025b.

Moisseev, D. N. and Chandrasekar, V.: Examination of the $\mu$–$\Lambda$ Relation Suggested for Drop Size Distribution Parameters, Journal of Atmospheric and Oceanic Technology, https://doi.org/10.1175/JTECH2010.1, 2007.

Myagkov, A., Kneifel, S., and Rose, T.: Evaluation of the reflectivity calibration of W-band radars based on observations in rain, Atmospheric Measurement Techniques, 13, 5799–5825, https://doi.org/10.5194/amt-13-5799-2020, publisher: Copernicus GmbH, 2020.

OTT HydroMet GmbH: Operating instructions Present Weather Sensor OTT Parsivel$^2$, https://www.ott.com/products/meteorological-sensors-26/ott-parsivel2-laser-weather-sensor-2392/, 2017.

Sekelsky, S. M.: Near-Field Reflectivity and Antenna Boresight Gain Corrections for Millimeter-Wave Atmospheric Radars, Journal of Atmospheric and Oceanic Technology, https://journals.ametsoc.org/view/journals/atot/19/4/1520-0426_2002_019_0468_nfraab_2_0_co_2.xml, 2002.

Sekelsky, S. M. and Clothiaux, E. E.: Parallax Errors and Corrections for Dual-Antenna Millimeter-Wave Cloud Radars, Journal of Atmospheric and Oceanic Technology, https://journals.ametsoc.org/view/journals/atot/19/4/1520-0426_2002_019_0478_peacfd_2_0_co_2.xml, 2002.

Testud, J., Oury, S., Black, R. A., Amayenc, P., and Dou, X.: The Concept of "Normalized" Distribution to Describe Raindrop Spectra: A Tool for Cloud Physics and Cloud Remote Sensing, Journal of Applied Meteorology and Climatology, https://journals.ametsoc.org/view/journals/apme/40/6/1520-0450_2001_040_1118_tcondt_2.0.co_2.xml, 2001.

Tokay, A., Wolff, D. B., and Petersen, W. A.: Evaluation of the New Version of the Laser-Optical Disdrometer, OTT Parsivel2, Journal of Atmospheric and Oceanic Technology, https://doi.org/10.1175/JTECH-D-13-00174.1, 2014.

Tridon, F., Battaglia, A., Luke, E., and Kollias, P.: Rain retrieval from dual-frequency radar Doppler spectra: validation and potential for a mid-latitude precipitating case-study, Quarterly Journal of the Royal Meteorological Society, 143, 1364–1380, https://doi.org/10.1002/qj.3010, _eprint: https://onlinelibrary.wiley.com/doi/pdf/10.1002/qj.3010, 2017.

https://doi.org/10.5194/egusphere-2026-507
Preprint. Discussion started: 29 January 2026


Tukiainen, S., O'Connor, E., and Korpinen, A.: CloudnetPy: A Python package for processing cloud remote sensing data, Journal of Open Source Software, 5, 2123, https://doi.org/10.21105/joss.02123, 2020.

Tukiainen, S., Siipola, T., Anniina, K., and O'Connor, E.: CloudnetPy: A Python package for processing cloud remote sensing data, https://doi.org/10.5281/zenodo.13833101, 2024.

Ulbrich, C. W. and Atlas, D.: Rainfall Microphysics and Radar Properties: Analysis Methods for Drop Size Spectra, Journal of Applied Meteorology and Climatology, https://journals.ametsoc.org/view/journals/apme/37/9/1520-0450_1998_037_0912_rmarpa_2.0.co_2.xml, 1998.

Wielaard, D. J., Mishchenko, M. I., Macke, A., and Carlson, B. E.: Improved T-matrix computations for large, nonabsorbing and weakly absorbing nonspherical particles and comparison with geometrical-optics approximation, Applied Optics, 36, 4305–4313, https://doi.org/10.1364/AO.36.004305, publisher: Optica Publishing Group, 1997.

Williams, C. R.: How Much Attenuation Extinguishes mm-Wave Vertically Pointing Radar Return Signals?, Remote Sensing, 14, 1305, https://doi.org/10.3390/rs14061305, number: 6 Publisher: Multidisciplinary Digital Publishing Institute, 2022.

Williams, C. R., Gage, K. S., Clark, W., and Kucera, P.: Monitoring the Reflectivity Calibration of a Scanning Radar Using a Profiling Radar and a Disdrometer, Journal of Atmospheric and Oceanic Technology, https://doi.org/10.1175/JTECH1759.1, 2005.

Wong, R. K. W. and Chidambaram, N.: Gamma Size Distribution and Stochastic Sampling Errors, Journal of Applied Meteorology and Climatology, 24, 568 – 579, https://doi.org/10.1175/1520-0450(1985)024<0568:GSDASS>2.0.CO;2, 1985.